

Article

Vancomycin-Conjugated Polyethyleneimine-Stabilized Gold Nanoparticles Attenuate Germination and Show Potent Antifungal Activity against *Aspergillus* spp.

Aishwarya Nikhil ^{1,†}, Atul Kumar Tiwari ^{2,†}, Ragini Tilak ¹, Saroj Kumar ³, Prahlad Singh Bharti ³, Prem C. Pandey ², Roger J. Narayan ^{4,*} and Munesh Kumar Gupta ^{1,*}

¹ Mycology Research Group, Department of Microbiology, Institute of Medical Sciences, Banaras Hindu University, Varanasi 221005, India; aishwaryanikhil1995@gmail.com (A.N.); tilakragini28@gmail.com (R.T.)

² Department of Chemistry, Indian Institute of Technology (BHU), Varanasi 221005, India; atulkumartiwari.rs.chy19@itbhu.ac.in (A.K.T.); pcpandey.apc@itbhu.ac.in (P.C.P.)

³ Department of Biophysics, All India Institute of Medical Sciences, New Delhi 110029, India; sarojgupta.k@gmail.com (S.K.); bharti.pbh@gmail.com (P.S.B.)

⁴ Joint Department of Biomedical Engineering, University of North Carolina, Chapel Hill, NC 27599, USA

* Correspondence: roger_narayan@unc.edu (R.J.N.); muneshg.micro@bhu.ac.in (M.K.G.)

† These authors contributed equally to this work.

Abstract: Antifungal drug resistance in filamentous fungi, particularly *Aspergillus* species, is increasing worldwide. Therefore, new antifungal drugs or combinations of drugs are urgently required to overcome this public health situation. In the present study, we examined the antifungal activity of vancomycin-functionalized AuNPs. These functionalized AuNPs were characterized, and their antifungal activity and associated killing mechanism were investigated using conventional methodologies against the conidia of *A. fumigatus* and *A. flavus*. The differential antifungal activity of vancomycin-functionalized Au-NPs against the conidia of *Aspergillus* species is dependent on structural differences in the conidial cell wall. The results demonstrated potent fungicidal activity against *A. fumigatus*, with a MIC value of 4.68 µg/mL, 93% germination inhibition, and 38.4% killing rate within 8 h of exposure. However, the activity against *A. flavus* was fungistatic; a MIC value of 18.7 µg/mL and 35% conidial germination inhibition, followed by 28.4% killing rate, were noted under similar conditions. Furthermore, endogenous reactive oxygen species (ROS) accumulation was 37.4 and 23.1% in conidial populations of *A. fumigatus* and *A. flavus*, respectively. Raman spectroscopy analysis confirmed the possible (but not confirmed) binding of functionalized AuNPs with the chitin and galactomannan components of the cell wall. A potential strategy that involves the exploration of antibacterial drugs using AuNPs as efficient drug carriers may also be appropriate for countering emerging drug resistance in filamentous fungi.

Keywords: vancomycin; polyethyleneimine; functionalized gold nanoparticles; antifungal activity

Citation: Nikhil, A.; Tiwari, A.K.; Tilak, R.; Kumar, S.; Bharti, P.S.; Pandey, P.C.; Narayan, R.J.; Gupta, M.K. Vancomycin-Conjugated Polyethyleneimine-Stabilized Gold Nanoparticles Attenuate Germination and Show Potent Antifungal Activity against *Aspergillus* spp. *Appl. Sci.* **2024**, *14*, 6926. <https://doi.org/10.3390/app14166926>

Academic Editor: Andrey Miroshnichenko

Received: 2 July 2024

Revised: 26 July 2024

Accepted: 5 August 2024

Published: 7 August 2024



Copyright: © 2024 by the authors. Licensee MDPI, Basel, Switzerland. This article is an open access article distributed under the terms and conditions of the Creative Commons Attribution (CC BY) license (<https://creativecommons.org/licenses/by/4.0/>).

1. Introduction

Aspergillus is a saprophytic mold and the causative agent of aspergillosis. It is ubiquitous in indoor and outdoor air; most people inhale fungal spores daily. There are 180 species of *Aspergillus*, of which *A. fumigatus* and *A. flavus* are the most commonly described challenges to human health. *Aspergillus* species cause allergic bronchopulmonary aspergillosis (ABPA), a life-threatening invasive fungal infection [1]. A study estimated that 2.5% of adults with asthma are also infected with ABPA; this population includes around 4.8 million patients around the world [2]. Of these 4.8 million people, 4 million suffer from chronic pulmonary aspergillosis (CPA) [2]. An additional 1.2 million people are estimated to have experienced CPA after encountering tuberculosis [3];

more than 70,000 people have experienced CPA as a complication associated with sarcoidosis [4]. The form of aspergillosis associated with the most significant morbidity is invasive aspergillosis (IA), which is uncommon among healthy individuals; however, immunocompromised individuals are highly susceptible. The first population-based estimation of IA was performed in the San Francisco Bay Area in 1992–1993; this study indicated an annual incidence of 1–2 cases of aspergillosis per 100,000 people [5]. However, the incidence of IA infections has shifted, owing to an increase in organ transplants and stem cell transplants, as well as the introduction of newer immunosuppressive agents. The number of IA-infected patients increased in the United States by an average of 3% per year from 2000 to 2013 [6]. In 2014, nearly 15,000 patients in the United States were diagnosed with aspergillosis. This condition was associated with an estimated \$1.2 billion in economic loss [7].

A situation with high morbidity and mortality was encountered by patients with Coronavirus Disease 2019 (COVID-19) and secondary fungal infections, particularly mucormycosis and aspergillosis [8–10]. The frequent use of corticosteroids, immunosuppressive agents, central venous catheters (CVC), and mechanical ventilation increases the risk factors for secondary infections [11]. *A. fumigatus* has been described as the main cause of secondary fungal infections in critically ill COVID-19 patients [12]. Fungal coinfections in COVID-19 patients are associated with a higher mortality rate (of up to 83%) in spite of the provision of antifungal treatment [13]. The treatment of *Aspergillus* species is gaining additional attention from the research community due to the rapid emergence of antifungal drug resistance. In 2019, the CDC placed azole-resistant *A. fumigatus* on a watch list in its annual antimicrobial drug resistance report [14,15]. The approved therapeutics to combat aspergillosis include three types of antifungal agents, namely polyenes, triazoles, and echinocandins. However, the continued use of triazole agents against *Aspergillus* spp. has led to a greater occurrence of triazole-resistant strains. Studies suggest that triazole-resistant IA infection is significantly associated with treatment failure, with a mortality rate of 30–90%, depending on the patient type [16]. Similarly, voriconazole resistance has also been reported to be associated with an overall mortality of 21–25% in patients infected with IA [16]. However, relatively little is known about the amphotericin B susceptibility patterns of *A. fumigatus* in many parts of the world. Therefore, it is important to discover or develop new antifungal therapeutics as substitutes to conventional drugs to counter life-threatening fungal infections.

Nanotechnology offers tools to treat communicable and non-communicable diseases via novel mechanisms. For example, many researchers have considered the use of nanoparticles as drug carriers. The nanoparticles are straightforward to manipulate; their properties (e.g., size, shape, and surface chemistry) make these materials versatile platforms for treating bacterial and fungal infections [17,18]. In addition, owing to their high drug-loading efficiency and ability to cross biological membranes, selectively surface-tuned nanoparticles may serve as antimicrobial drug carriers for delivering drugs at the site of infection [19,20]. The capability of nanoparticles to interact with bacterial cells depends on the surface charge of the engineered nanoparticles; appropriate consideration of this parameter can increase the efficacy of the nano system against the pathogen. Various metal nanoparticles, such as silver, gold, zinc oxide, titanium dioxide aluminum oxide, and copper oxide nanoparticles, have been rigorously evaluated, either alone or conjugated with antibiotics and other functional molecules, for their potential to treat bacterial and fungal infections [21,22]. Among these, AuNPs have drawn significant interest because of their low cellular toxicity, attractive optical properties, and straightforward functionalization with appropriate drug molecules [23]. Recent studies have evaluated utilizing AuNPs as drug carriers for antimicrobial agents [24,25]. AuNPs can efficiently deliver relatively high drug concentrations at the site of infection with negligible cytotoxicity. For example, Lee et al. noted that the combination of AuNPs with ciprofloxacin or cefotaxime provided synergistic activity against *Salmonella* species through the induction of bacterial apoptosis-like phenomena [26]. Similarly, Fuller et al.

noted that colistin-conjugated AuNPs significantly enhanced the antibacterial efficacy of colistin against *E. coli*, providing a six-fold reduction in the minimum inhibitory concentration value when compared to colistin alone [27]. Furthermore, several studies have been conducted to increase the effectiveness of antifungal drugs by loading AuNPs, and these structures have potential uses in treating fungal infections. Several approaches have been developed to counter antifungal drug resistance in fungal strains by conjugating drugs or small molecules to enhance their killing efficiency. For example, indolicidin was conjugated with gold nanoparticles, and its efficacy was evaluated using fluconazole-resistant clinical isolates of *C. albicans* [28]. Vancomycin has a unique mode of action, which involves the inhibition of the second stage associated with cell wall synthesis in susceptible bacteria [29]. The inter-domain exploration of the antifungal activity of classical antibacterial drugs has not been considered. However, one study considered vancomycin as a biofilm inhibitor in synergy with other antibiotics against mature *Candida* biofilms [30].

The present work explores the synthesis of water-dispersible gold nanoparticles functionalized with vancomycin and evaluates their in vitro antifungal activity against *A. fumigatus* and *A. flavus*; the underlying mechanisms of action were also evaluated. To achieve this, we utilized polyethyleneimine to stabilize the gold nanoparticles and incorporated vancomycin as the drug payload. This study offers a potential solution to address antifungal drug resistance by integrating conventional antibacterial agents into gold nanocarriers for enhanced drug delivery and an approach to screen the antibacterial drug as antifungals.

2. Material and Methods

2.1. Materials

All the materials and reagents that were utilized in this study were of good analytical quality. Vancomycin, polyethyleneimine, chloroauric acid trihydrate, and voriconazole were acquired from Sigma-Aldrich (St. Louis, MO, USA). Sabouraud dextrose agar (SDA) and Roswell Park Memorial Institute RPMI-1640 (Buffalo, NY, USA) agar were purchased from HiMedia Laboratories Limited (Mumbai, Maharashtra, India). Other solvents were acquired from Merck Life Science Private Limited (Bangalore, Karnataka, India). Other glassware and plasticware were obtained from Tarson Products Private Limited (Kolkata, West Bengal, India). All experiments were undertaken using ultra-purified HPLC-grade water.

This study used the ATCC strains of *A. fumigatus* (204305) and *A. flavus* (204304) (American Type Culture Collection, Manassas, VA, USA). The fungal strains were identified by a conventional mycological procedure, including cultural and morphological features. The strains were subcultured on potato dextrose agar (PDA) and stored at $-20\text{ }^{\circ}\text{C}$ for further experiments.

2.2. Harvesting of Fungal Conidia

The preserved culture was subcultured on a Sabouraud dextrose agar (SDA) slant at $27\text{ }^{\circ}\text{C}$ for 4–6 days, and the conidia of *A. fumigatus* and *flavus* were harvested according to the method described by Singh et al. (2011) [31]. Briefly, 10 mL of 0.9% saline solution was added to a slant tube; this step was followed by the addition of 20–30 μL of Tween-20. The obtained suspension was collected and then centrifuged at 3500 rpm for 6 min, washed using 0.1 M PBS (pH 7.2), and resuspended in 0.9% saline. The conidia were counted with a Neubauer hemocytometer, and the results were expressed as conidia/mL for further experiments.

2.3. Synthesis and Physical Characterization of Functionalized Nanoparticles

PEI-stabilized gold nanoparticles were synthesized according to a previously reported procedure with slight modifications [32,33]. In brief, 800 μL (10 mM) of

tetrachloroauric acid ($\text{HAuCl}_4 \cdot 3\text{H}_2\text{O}$) was placed in a 2 mL glass vial; this step was followed by the addition of an aqueous vancomycin solution (50 μL , 2 mg/mL stock solution). The reaction mixture was stirred using a magnetic stirrer over a period of 5–10 min; an aqueous solution of polyethyleneimine (50 μL of 4 mg/mL stock solution) was subsequently added. The reaction mixture was mixed with a stirrer; this step was followed by the addition of 20 μL formaldehyde. The stirring process was continued for 30 min, which yielded a dark red-pink color PEI-AuNP@Van. A final ratio was maintained as 2:2:4 for gold cation, vancomycin, and polyethyleneimine, respectively.

Spectroscopic and micrographic methods were used to characterize the synthesized PEI-AuNP@Van. UV-VIS spectroscopy was conducted using a Hitachi U-2900 spectrophotometer (Hitachi Hi-Tech, Tokyo, Japan). Transmission electron microscopy (TEM) was performed using a Technai G2 20 S TWIN instrument (FEI, Hillsboro, OR, USA) to determine shape and size. The average size of PEI-AuNP@Van was examined with ImageJ software (National Institutes of Health, Bethesda, MD), and a statistical graph was plotted using Origin 8.5 software (Northampton, MA, USA). Fluorescence emission (FL emission) spectroscopy data were acquired using a Hitachi F7000 fluorescence spectrophotometer (Hitachi Hi-Tech, Tokyo, Japan), and a Malvern Nano Zeta Sizer (Malvern, UK) was utilized in order to obtain dynamic light scattering and zeta potential data.

2.4. Antifungal Evaluation and Minimal Inhibitory Concentration (MIC) Determination

The minimum inhibitory concentration (MIC) of PEI-AuNP@Van against *A. fumigatus* and *A. flavus* conidia ($0.5\text{--}5 \times 10^3$ conidia/mL) was determined by applying a two-fold serial dilution approach in a sterile, 96 well, flat-bottom microtiter plate as described previously [34]. Briefly, an active suspension of 150 $\mu\text{g}/\text{mL}$ PEI-AuNP@Van or PEI-AuNPs was prepared. One hundred microliters of each solution were dispensed in the first well and serially diluted; the final concentration was between 0.58 and 150 $\mu\text{g}/\text{mL}$. Similarly, the positive control (voriconazole and vancomycin; 32 $\mu\text{g}/\text{mL}$ each) and negative control (distilled water) were serially diluted. Next, 100 μL of conidial suspension was added to each well. Next, the microtiter plate was incubated in a static position at 35 °C for 24 h; a visual demonstration of turbidity (e.g., the presence of a visually clear well) was corroborated by the MIC value. Subsequently, a 10 μL aliquot that was obtained from each well was subcultured on SD agar plates for 72 h, and fungal growth was examined. The MIC data were assessed as corresponding to the concentration of the initial gold cations irrespective of the concentration of vancomycin.

2.5. Studies on Germination Attenuation of *Aspergillus* Conidia

A. fumigatus and *A. flavus* conidia were prepared as previously discussed. The conidial germination inhibition assay was undertaken as previously described [35]. Then, 100 μL of spore suspension (10^6 conidia/mL) was mixed with PEI-AuNP@Van at their respective MIC, and the control samples (positive control and negative control) contained 50 μL (1.2 $\mu\text{g}/\text{mL}$) of voriconazole and 50 μL of distilled water. Samples (50 μL) were extracted from each tube, transferred to a sterile concave slide, and incubated at 35 °C for 8 h. One hundred spores per treatment were evaluated at defined intervals of 48 h. The observation was made with the help of a bright-field binocular compound light microscope (Olympus, Tokyo, Japan). The percentage germination inhibition rate was evaluated using the following equation [35]:

$$\text{Spore germination rate (\%)} = \frac{(\text{the number of germinated spores})}{(\text{the total number of spores})} \quad (1)$$

2.6. Laser Scanning Confocal Microscopy for the Assessment of Conidial Viability

The viability of PEI-AuNP@Van-treated conidia of *A. fumigatus* and *A. flavus* was assessed using a membrane-impermeable dye, propidium iodide (PI), and visualized using laser scanning super-resolution confocal microscopy [35]. Briefly, 5 mL of freshly prepared conidial suspension was prepared as previously described and treated with 100 μ L of PEI-AuNP@Van at its MIC value, along with positive controls and negative controls (voriconazole and distilled water, respectively) for 8 h at 35 °C. A 1 mL aliquot was taken 8 h after each test tube and centrifuged for 5 min at 3500 rpm. The pellet obtained was washed twice using PBS (0.1 M) and resuspended in PBS. The conidia were stained with 10 μ L (1 mg/mL stock) of PI (excitation/emission at 535/617 nm), incubated in the dark at room temperature for 30 min, and washed again with PBS to eliminate any excess dye. Subsequently, the treated samples were examined using an SP5 AOBs super-resolution confocal laser-scanning microscope (Leica, Wetzlar, Germany) with a 40 \times immersion oil objective. The anti-*Aspergillus* activity of PEI-AuNP@Van was confirmed by the fact that dead conidia (damaged cell membranes) stained with PI and live conidia remained unstained because an intact plasma membrane prevented the internalization of PI within the cell [35].

2.7. Fluorescence Activated Cell Sorting (FACS)

To determine the percentage of dead conidia after an 8 h treatment, conidial suspensions of *A. fumigatus* and *A. flavus* were prepared as previously described in the literature [35, 36]. Five milliliters of culture were mixed with 10⁶ conidia/mL in RPMI-1640 medium, followed by the addition of PEI-AuNP@Van at the respective MIC values. Positive controls and negative controls were prepared in separate tubes, and all tubes were incubated for 8 h at 35 °C. After incubation, aliquots were centrifuged at 3500 rpm for 6 min. The pellet was washed using PBS and resuspended using PBS. The treated conidia were stained with 10 μ L PI (1 mg/mL stock solution) (excitation/emission, 535 nm/617 nm), incubated for 30 min at room temperature in the dark, and washed with PBS to eliminate any excess stain. Data acquisition was performed using a BD FACSAria Fusion flow cytometer (BD Biosciences, San Diego, CA, USA) based on the light scatter and fluorescence signals from 20 mW laser illumination (λ = 488 nm). All of the measurements were conducted logarithmically. The assay was undertaken at a low sample rate (14- μ L min⁻¹). In total, 10⁴ events were considered for each sample.

2.8. Endogenous Reactive Oxygen Species (ROS) Accumulation Study

Endogenous reactive oxygen species (ROS) production in *A. fumigatus* and *A. flavus* conidia after exposure to PEI-AuNP@Van for 8 h was monitored using flow cytometry with 2', 7'-dichlorofluorescein-diacetate (DCFH-DA) as a ROS marker, as described previously [37]. After exposure for 8 h, the conidia were pelleted and washed twice with phosphate-buffered saline (PBS, pH ~ 7.2); the conidial density was adjusted to 10⁶/mL by suspending in PBS. The resuspended conidia were incubated with 5 μ M DCFH-DA for 30 min; ROS accumulation was analyzed using a BD FACSAria Fusion flow cytometer (BD Biosciences, San Jose, CA, USA). Data acquisition was conducted using the BD Accuri C6 software using light scattering and fluorescence signals from a 20 mW laser illumination (λ = 488 nm). All of the measurements were conducted logarithmically. The assay was conducted at a low sample rate (14 μ L min⁻¹). For each sample, a total of 10⁴ events were taken into account [37].

2.9. Raman Spectroscopy Studies

Raman spectroscopy was performed to investigate biomolecular changes in conidia after exposure to PEI-AuNP@Van, untreated samples, and voriconazole against *A. fumigatus* and *A. flavus*. PEI-AuNP@Van, untreated samples, and voriconazole-exposed conidia were pelleted and washed twice with PBS in order to remove debris. The samples

were then placed on microscopic glass slides and dried for 30 min at ambient temperature. Raman measurements were performed using a CRM Alpha 300 instrument (WiTec GmbH, Germany). The excitation source used in this study was a Nd-YAG laser that was operated at 532 nm; the maximum power output associated with the laser was 40 mW. At the sampling point, the laser power was reduced to approximately 16 mW. The dispersed intensity of the light of the signal from the grating was determined using a Peltier-cooled charge-coupled-device (CCD), and the spectrum was recorded in the window of 400–1800 cm^{-1} .

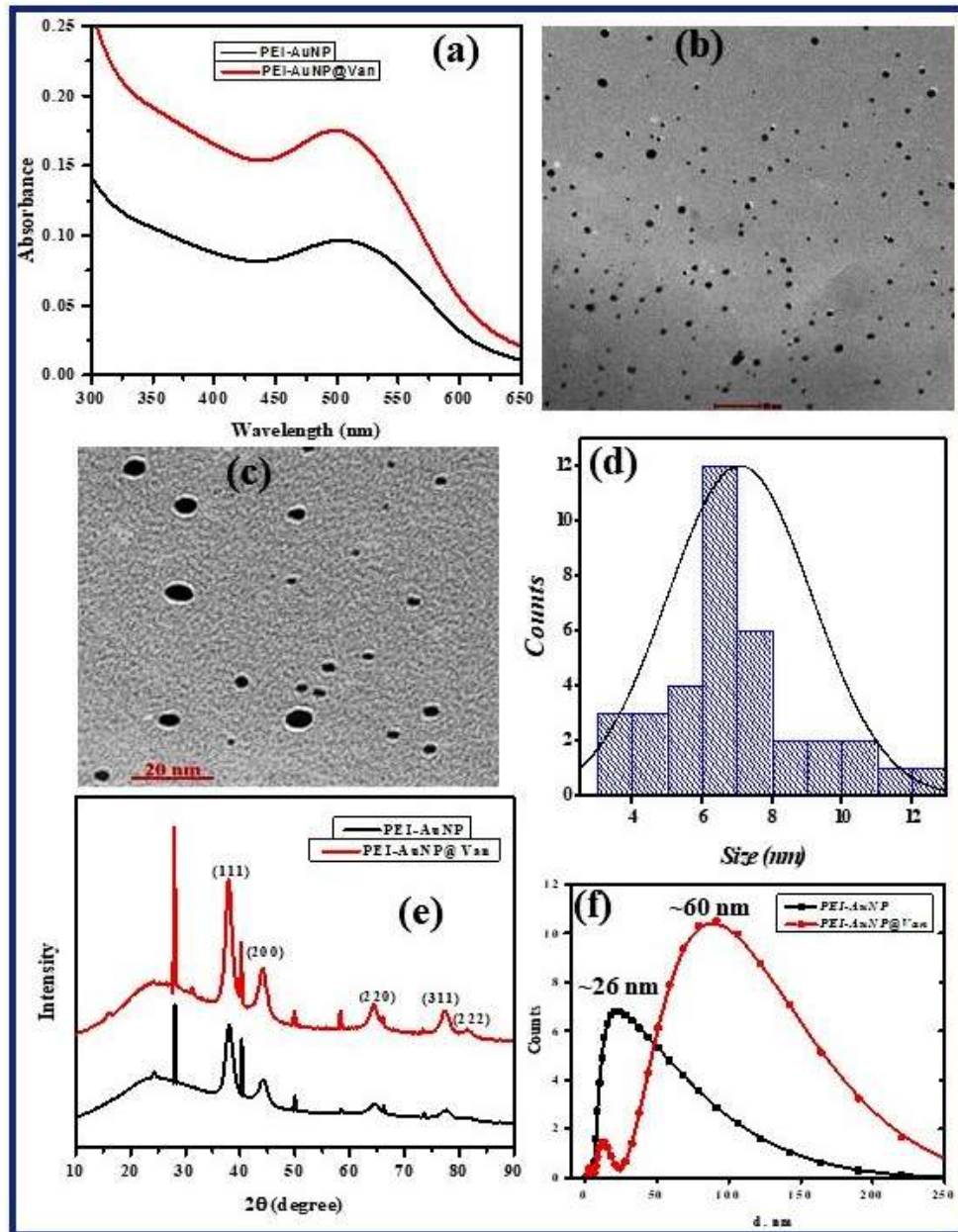
2.10. TEM Characterization of PEI-AuNP@Van Treated Conidia

For TEM characterization, freshly harvested conidia of *A. fumigatus* and *A. flavus* were prepared, treated with PEI-AuNP@Van at their respective MIC values, and incubated for 8 h at 35 °C. After 8 h of exposure, the culture was pelleted, washed with PB, and fixed with Karnowsky solution for 1 h. The control and treated samples were drop-cast on a carbon-coated copper grid with a mesh size of 300 μm and dried under ambient conditions for 1 h. Visualization was performed using a Tecnai G2 20 S TWIN TEM instrument (FEI, Hillsboro, OR, USA).

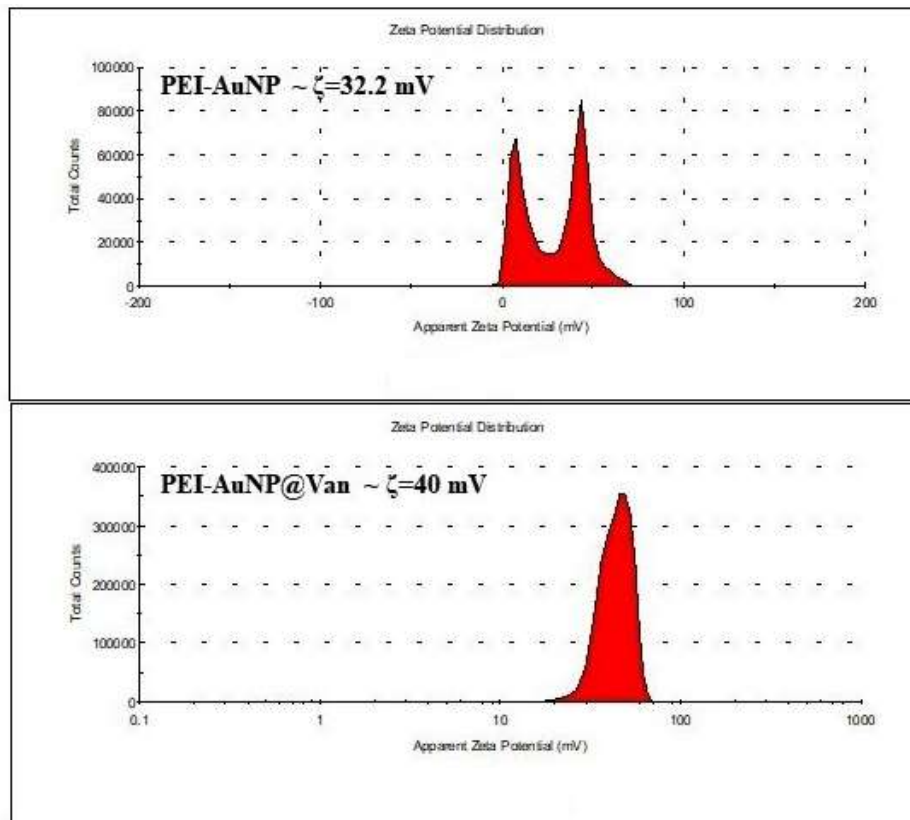
3. Results

3.1. Synthesis and Characterization of Vancomycin-Functionalized Gold Nanoparticles

The synthesized vancomycin-functionalized and non-functionalized AuNPs (PEI-AuNP@Van and PEI-AuNPs) were evaluated using a UV-Vis spectrophotometer, and a strong SPR signal was observed at 515 nm (Figure 1(Aa)), which is consistent with the characteristic SPR value of AuNPs. Notably, PEI-AuNP@Van demonstrated a high absorbance and a sharp spectrum compared to PEI-AuNPs. TEM characterization confirmed that PEI-AuNP@Van had an actual size of ~7 nm (Figure 1(Ab,d)). Figure 1(Ac) revealed the presence of a surface coating of vancomycin and PEI molecules, confirming the presence of surface functionalization. The crystallinity and diffraction angles of the synthesized PEI-AuNPs and PEI-AuNP@Van were investigated by XRD at angles between 10° and 80°. Figure 1(Ae) shows the assigned peaks for PEI-AuNPs and PEI-AuNP@Van; the peaks at 38.4°, 44.6°, 64.6°, and 77.7° correspond to the (111), (200), (220), and (311) lattice planes, respectively. The peak located at 38.4° was of a higher intensity than the other peaks; these results confirmed the face-centered unit cell (FCC) structure of the material. The hydrodynamic radii of PEI-AuNP@Van were recorded, which showed a value of ~58 nm; the value for PEI-AuNPs was ~23 nm (as indicated in Figure 1(Af)). The increase observed in the hydrodynamic radii indicates the functionalization of vancomycin. As indicated in Figure 1B, the zeta potential of PEI-AuNPs was ~+32.2 mV; however, when PEI-AuNP@Van was functionalized with vancomycin (PEI-AuNP@Van), the surface charge increased to ~40 mV. This increase in zeta potential is in agreement with the high stability of the nanoparticles.



(A)



(B)

Figure 1. (A) Physical characterization of PEI-AuNP@Van nanoparticles. (a) UV-Vis spectrum, (b) TEM micrograph, (c) high resolution image of nanoparticles, (d) mean nanoparticle size, (e) XRD diffractogram, and (f) dynamic light scattering data. (B) Zeta potential distribution histograms for non-functionalized gold nanoparticles (PEI-AuNPs) and vancomycin-functionalized gold nanoparticles (PEI-AuNP@Van).

3.2. Confirmation of Vancomycin Functionalization on Gold Nanoparticles by Using Fluorescence Spectroscopy

Vancomycin is a fluorescent antibiotic with an intense fluorescence emission at 335 nm when excited at 280 nm. The fluorescence characteristics of PEI-AuNPs and PEI-AuNP@Van were examined to confirm the functionalization of AuNPs with vancomycin [33]. The emission wavelengths (λ_{em}) of PEI-AuNPs, vancomycin, and PEI-AuNP@Van at an excitation wavelength of 280 nm are shown in Figure 2. For excitation at 280 nm, vancomycin exhibited intense emission at 335 nm, and PEI-AuNPs and PEI-AuNP@Van were observed at 380 and 420 nm, respectively. As shown in Figure 2, the emission wavelength of PEI-AuNP@Van shifted substantially, with a low-intensity peak at 300 and 335 nm and a high-intensity peak at 420 nm, indicating vancomycin functionalization on the gold nanoparticle surface, corroborating the TEM results shown in Figure 1(Ac).

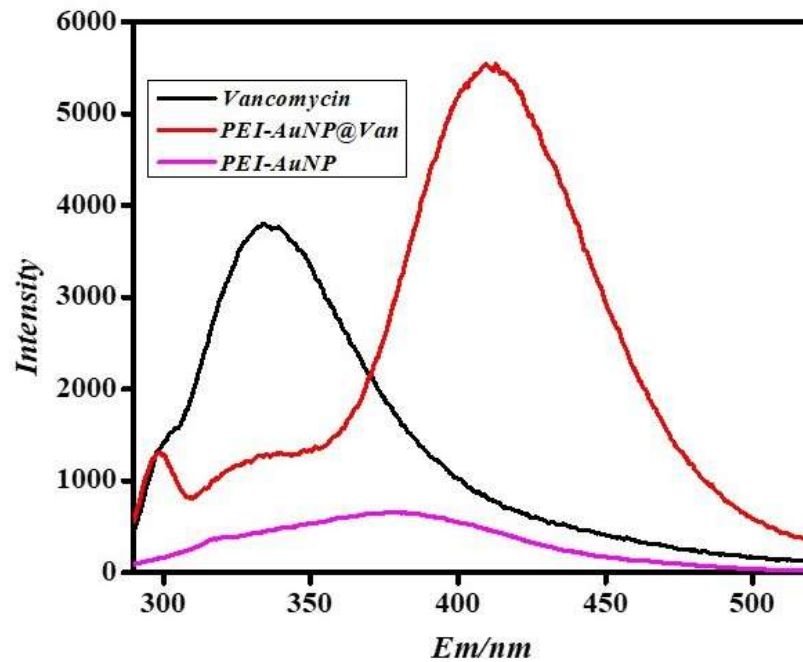


Figure 2. Fluorescence spectroscopic confirmation of vancomycin functionalization of PEI-stabilized gold nanoparticles. Adopted and modified under CC BY (2023) [33].

3.3. Antifungal Activity and Minimal Inhibitory Concentration (MIC)

The antifungal activity of vancomycin-functionalized gold nanoparticles (PEI-AuNP@Van) and non-functionalized gold nanoparticles (PEI-AuNPs) was assessed using the agar well diffusion method and by obtaining the minimum inhibitory concentration values of these materials. As shown in Figure 3a,b, the non-conjugated AuNPs and vancomycin did not show any zone of inhibition; however, the conjugated AuNPs demonstrated potent activity against *A. fumigatus* (Figure 3a). In addition, the material exhibited fungistatic activity against *A. flavus* (Figure 3b). The MIC values of PEI-AuNPs and PEI-AuNP@Van, along with voriconazole and vancomycin, against *A. fumigatus* and *A. flavus* were obtained using the broth microdilution method. The MIC values for PEI-AuNPs against *A. fumigatus* were higher than those for PEI-AuNP@Van; the values for PEI-AuNPs and PEI-AuNP@Van were 37.5 and 4.68, respectively. Notably, voriconazole and vancomycin provided MIC values of 1.2 $\mu\text{g}/\text{mL}$ and no activity, respectively. In contrast, The MIC values of PEI-AuNPs, PEI-AuNP@Van, voriconazole, and vancomycin against *A. flavus* were 75.0, 18.75, 1.5 $\mu\text{g}/\text{mL}$ and no activity, respectively (Figure 3). The higher MIC value of the non-functionalized AuNPs indicated an unusual role for vancomycin in germination inhibition and antifungal activity; however, vancomycin without conjugation did not show any effect on fungal growth. Owing to the high MIC of PEI-AuNPs and the ineffectiveness of vancomycin, the remaining studies were performed with PEI-AuNP@Van.

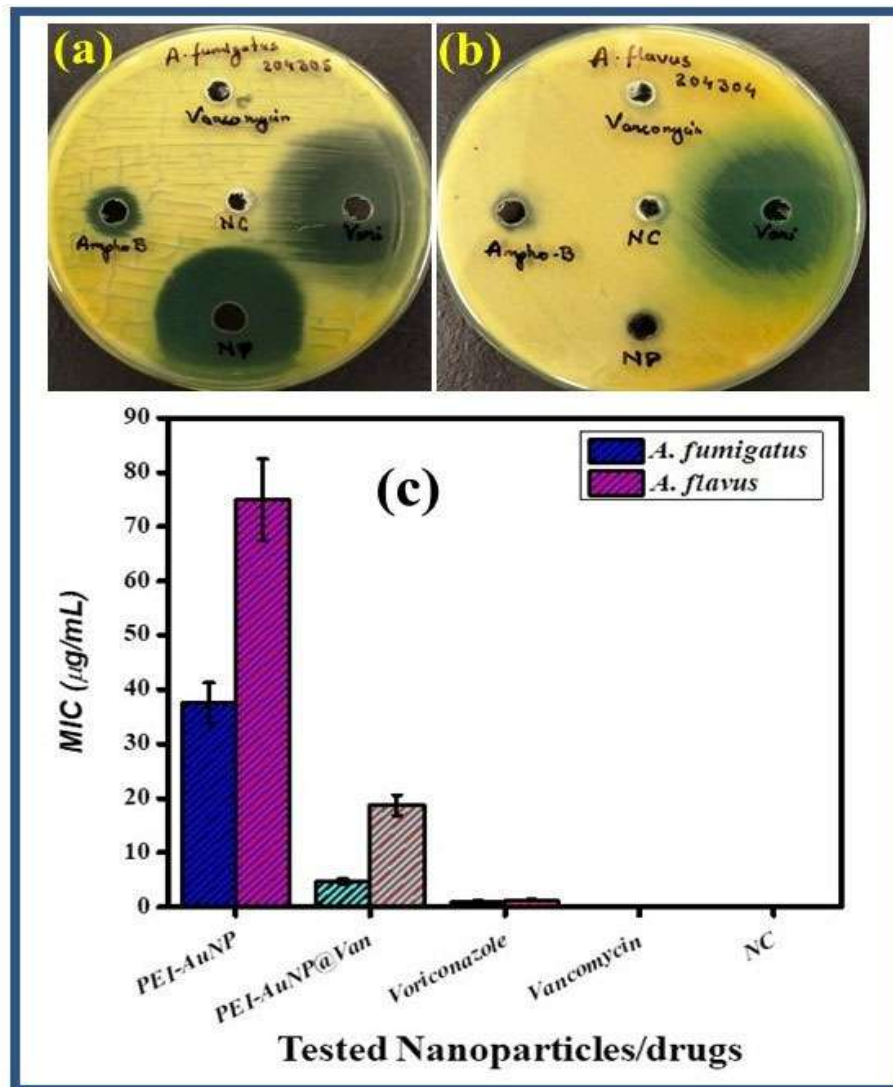


Figure 3. Antifungal evaluation plates (a) against *A. fumigatus* and (b) *A. flavus* (NC = PEI-AuNPs control; NP = PEI-AuNP@Van; PC = positive control). (c) MIC values of non-functionalized AuNPs (PEI-AuNPs), vancomycin-functionalized AuNPs (PEI-AuNP@Van), positive control (voriconazole), vancomycin, and negative control (DW) against *A. fumigatus* and *A. flavus*.

3.4. Germination Inhibition of Conidia by PEI-AuNP@Van

A germination inhibition assay was performed at different time intervals using voriconazole and PEI-AuNP@Van against the conidia of *A. fumigatus* and *A. flavus*. As mentioned earlier, this study demonstrated that the germination of the conidia was attenuated by PEI-AuNP@Van; variable dynamics against both fungal strains were demonstrated (Figures 4, S1 and S2). A germination inhibition study was conducted for 48 h at 4, 8, 12, 24, and 48 h intervals against the conidia of *A. fumigatus* and *A. flavus*. The results indicated that PEI-AuNP@Van attenuated the germination of *A. fumigatus* by 93%. In contrast, voriconazole inhibited growth by 56% after 48 h of treatment at its respective MIC values (as shown in Figures 4 and S1). Similarly, *A. flavus* conidial germination was inhibited by PEI-AuNP@Van by up to 35%; voriconazole inhibited *A. flavus* conidial germination by only 42% (as shown in Figures 4 and S2). Thus, PEI-AuNP@Van showed considerable potential as a germination attenuator against *A. fumigatus* compared with voriconazole.

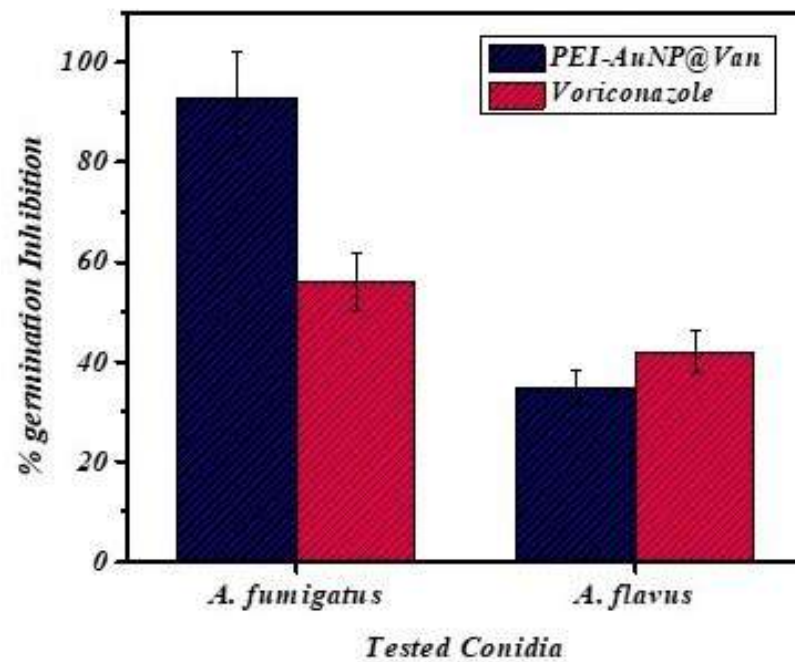


Figure 4. Conidial germination inhibition assay.

3.5. Conidial Viability Studies

The antifungal activities of PEI-AuNP@Van and voriconazole against *A. fumigatus* and *A. flavus* were investigated by super-resolution laser scanning confocal microscopy. The freshly prepared conidia of *A. fumigatus* and *A. flavus* were challenged with the respective MIC of PEI-AuNP@Van and voriconazole for 8 h, followed by staining using the red fluorescent dye propidium iodide and subsequent imaging, as shown in Figures 5, S3 and S4. The results confirmed that PEI-AuNP@Van could potentially compromise the cell membrane of *A. fumigatus* conidia compared to voriconazole. The percentage of dead conidia was calculated using fluorescence-activated cell sorting of the PEI-AuNP@Van-treated conidia for both strains stained with PI. After 8 h of treatment, 38.4% of the conidia of *A. fumigatus* were dead (Figure 6a,b); in contrast, only 28% of the conidia of *A. flavus* were dead (as shown in Figure 6c,d).

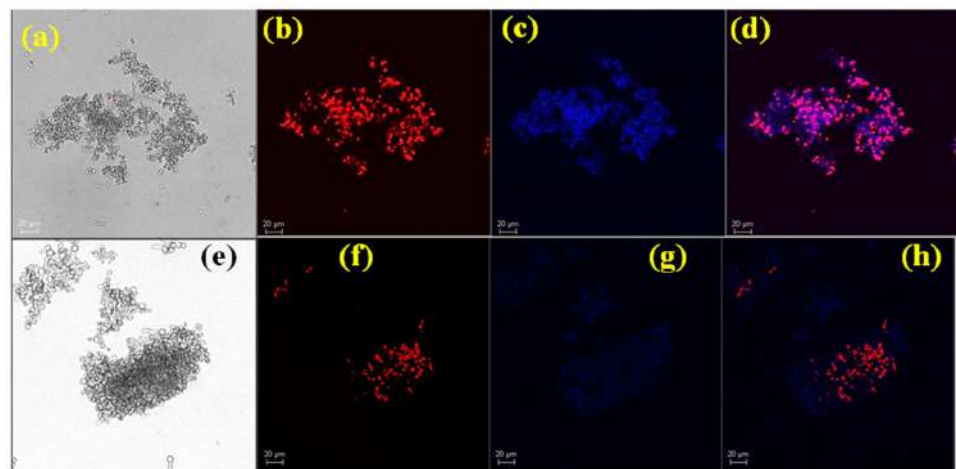


Figure 5. Confocal micrograph of PEI-AuNP@Van treated conidia of *Aspergillus*. (a) Bright field image of *A. fumigatus* treated with PEI-AuNP@Van and (b) stained with PI; (c) blue panel showing

surface adsorbed functionalized nanoparticles, and (d) merged panel; (e) bright field image of *A. flavus* treated with PEI-AuNP@Van and (f) stained with PI; (g) blue panel showing surface adsorbed functionalized nanoparticles, and (h) merged panel.

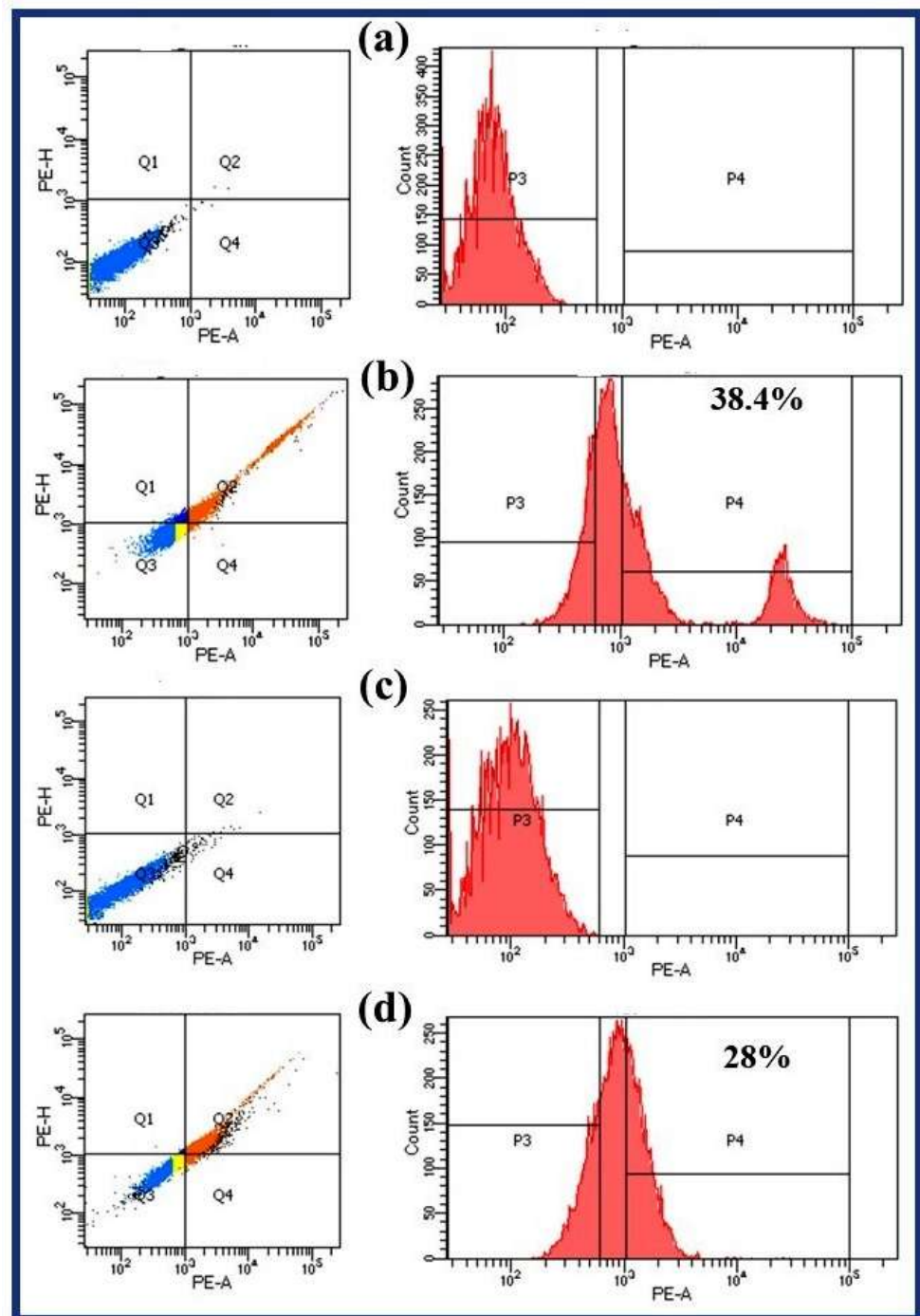


Figure 6. Histograms of dead conidia after 8 h of exposure to PEI-AuNP@Van. (a,c) represent the untreated controls of *A. fumigatus* and *A. flavus*, respectively; (b,d) represent PEI-AuNP@Van-treated conidia of *A. fumigatus* and *A. flavus*.

4. Antifungal Mechanism

4.1. Endogenous ROS Generation

The fungal conidia exposed to the PEI-AuNP@Van were examined for ROS generation using 2', 7'-dichlorofluorescein-diacetate (DCFH-DA) with flow cytometry. We noted significant differences in the ROS generation profile of PEI-AuNP@Van (Figure 7). PEI-AuNP@Van showed an increase in DCF fluorescence compared with that of the control (Figure 7a,c). Furthermore, the population shift was significant in the *A. fumigatus* (bimodal shift) and *A. flavus* conidial populations. After 8 h of exposure, 37.4% conidia of *A. fumigatus* (Figure 7b) and 23.1% of *A. flavus* (Figure 7d) exhibited ROS generation. This result shows that PEI-AuNP@Van significantly induced ROS generation.

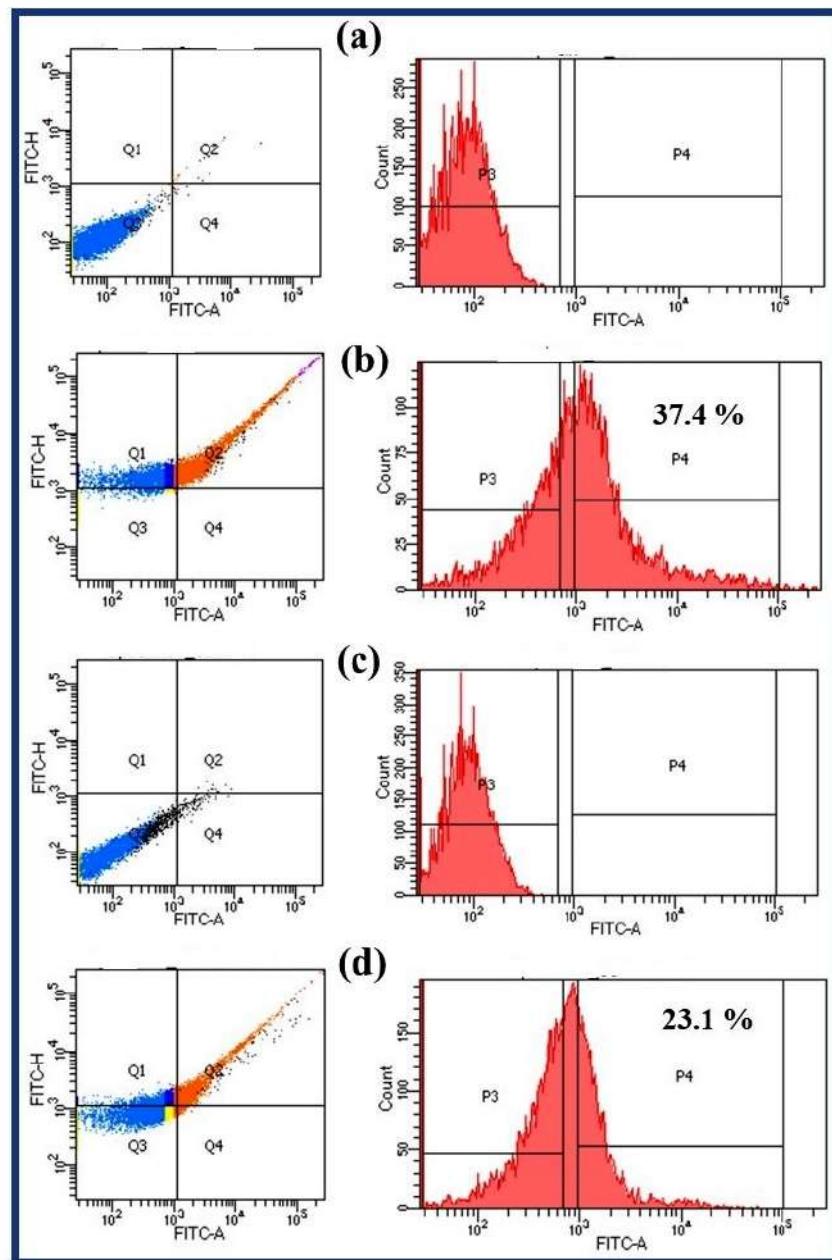


Figure 7. Endogenous ROS accumulation in PEI-AuNP@Van-treated conidia. (a,c) show the untreated control conidia of *A. fumigatus* and *A. flavus*, respectively; (b,d) represent the PEI-AuNP@Van-treated conidia.

4.2. Raman Spectroscopy Analysis

Aspergillus conidia possess a complex outer cell wall containing galactomannan, mannoproteins, chitin, and several sensory and architectural proteins. Thus, analysis of the Raman spectra can indicate structural changes in the conidial wall after nanoparticle exposure. Therefore, Raman spectrometry of the PEI-AuNP@Van-treated conidia was performed along with that of the untreated control. The recorded spectrum matched with previously characterized fingerprints of biomolecules; structural assignments by different research groups [38–47] concluded that there were significant architectural differences between the PEI-AuNP@Van-treated conidia and untreated conidia.

4.2.1. Raman Spectroscopy Analysis of PEI-AuNP@Van and Voriconazole-Treated *A. flavus* Conidia

The Raman spectra of the untreated PEI-AuNP@Van and voriconazole-treated conidia are shown in Figure 8, and the detailed spectrum assignments are shown in Table S1 (Supplementary File). The Raman spectrum of the untreated conidia of *A. flavus* exhibited peaks at 335 cm^{-1} (in-plane bending of CCO and torsion at COHO in galactomannan, an integral part of *A. flavus* cell wall), 422 cm^{-1} (in-plane bending of CCC, CCO, and OCO bonds), 559 cm^{-1} (in-plane bending of CCC), 1059 cm^{-1} (in-plane bending of COH/vibration of CO in ribose), 1250 cm^{-1} (scissoring in CH_2 /amide III random), 1347 cm^{-1} (D-fructose-6 phosphate), 1412 cm^{-1} (wagging of C-H in myristic acid/galactomannan), 1526 cm^{-1} (related to -C=C- stretching/vibration in the C-C bond of carotenoids), 1595 cm^{-1} (NH_2 deformation/amide III protein), and 1712 cm^{-1} (asymmetric vibration in CO_2 stretches) (Figure 8(ai)). These peaks were associated with a conidial cell wall composed of complex sugars and proteins such as mannoproteins, glucan, chitin, galactomannan, and ergosterol.

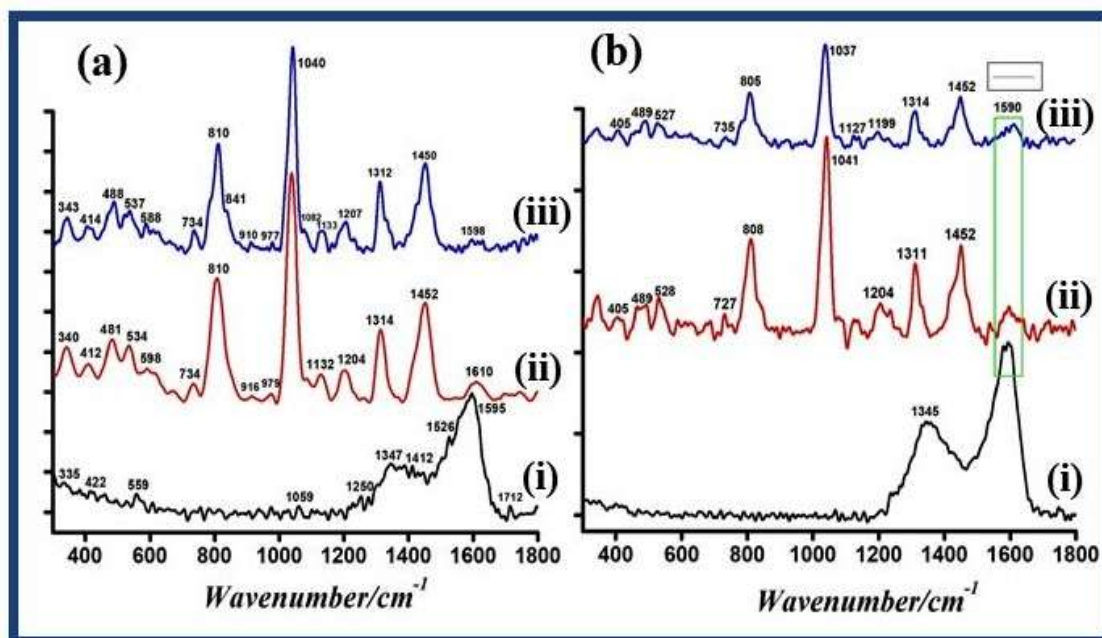


Figure 8. Raman spectra of voriconazole and PEI-AuNP@Van-treated conidia of *A. flavus* and *A. fumigatus* along with an untreated control. (ai) Untreated conidia of *A. flavus*, (aii) treated with voriconazole, (aiii) treated with PEI-AuNP@Van, (bi) untreated conidia of *A. fumigatus*, (bii) treated with voriconazole, and (biii) treated with PEI-AuNP@Van.

The effect of voriconazole on the *A. flavus* conidia was evaluated as a drug control. Voriconazole inhibits cytochrome P450-dependent 14α -lanosterol demethylation, an

important stage in fungal cell membrane ergosterol synthesis. This process ultimately destabilizes the cell membrane, leading to cellular fractures. The following peaks were observed in the Raman spectra (as shown in Figure 8(aii)): 340, 412, 481, 534, 598, 734, 810, 916, 979, 1040, 1132, 1204, 1314, 1452, and 1610 cm^{-1} . The functional groups and chemical bonds of the spectral band were tentatively assigned as follows: plane bending of the OH in chitin (340 cm^{-1}), amylopectin (412 cm^{-1}), in-plane bending in the CCC skeletal mode/glucosyl ring deformation (534 cm^{-1}), in-plane bending vibration of the pyranoid ring (598 cm^{-1}), and thymidine (734 cm^{-1}). In addition to the medium- and weak-intensity peaks, some firm peaks were observed (in contrast to the spectrum of untreated conidia) (Figure 8(ai)). These peaks can be assigned as follows: antisymmetric stretching in OPO phosphodiester (810 cm^{-1}), indicating external cell wall damage; out-of-plane bending of the benzene ring in phenylalanine (916 cm^{-1}); $\beta(\text{CCH})$ and $\beta(\text{CCO})$ /pyruvate (979 cm^{-1}); C–C stretching in phospholipids/tetradecanoic acid, carbohydrates (e.g., chi-tin), and C–N stretching (1040 cm^{-1}); $\nu(\text{CO})$ mode in the COC (unsaturated fatty acids in lipids/galactomannan) (1132 cm^{-1}); twisting in CH_2 /deformation mode in C–H of polysaccharide (1204 cm^{-1}); vibration in CN/wagging in CH_2 of tyrosine (1314 cm^{-1}); in-plane bending vibration of CH/wagging or deformation of CH_2 /in-plane bending vibration of OH (1452 cm^{-1}); and in-plane bending of NH/amide III of protein (1610 cm^{-1}).

The Raman spectrum of the PEI-AuNP@Van-treated conidia was similar to that of the voriconazole-treated conidia, indicating the surface binding of functionalized nanoparticles and cell wall damage, which supports the fungistatic behavior of PEI-AuNP@Van. Figure 8(aiii) shows the Raman spectrum of the PEI-AuNP@Van-treated *A. flavus* conidia for 8 h. When compared to the spectrum of the voriconazole-treated conidia (Figure 8(ai)), it was observed that some spectral peaks were slightly shifted towards both lower and higher wave numbers. This shift can be attributed to changes in the chemical bond length. Shifting to a higher wave number denotes a reduction in the chemical bond length and vice versa. Based on the observed spectral bands, the assignments are as follows: the band at 340 cm^{-1} in the voriconazole-treated conidia was shifted to 343 cm^{-1} in PEI-AuNP@Van treated conidia, indicating a shortening of the OH bond in chitin. Similarly, the peak at 412 cm^{-1} shifted slightly to 414 cm^{-1} , indicating significant structural changes in cell wall carbohydrates. The peak at 481 cm^{-1} shifted to 488 cm^{-1} ; this peak can be assigned to the in-plane bending vibration of CO-NH/C-CH₃ in galactomannan and chitin. Again, the peak at 534 cm^{-1} shifted to 537 cm^{-1} ; this result can be assigned to glucofuranose ring deformation. A new Raman peak at 588 cm^{-1} , which was observed in the PEI-AuNP@Van-treated conidia, was tentatively assigned to the in-plane bending of CCO in the fructosyl ring. Some typical peaks (734, 810, and 1040 cm^{-1}) were observed in the spectra of the voriconazole- and PEI-AuNP@Van-treated conidia (Figure 8(aii,aiii)). A weak peak at 841 cm^{-1} , which was linked to an intense peak at 810 cm^{-1} , can be assigned to CO/CC/CH deformation, suggesting the exposure of DNA/RNA/phospholipids. Furthermore, Raman shifts were observed at 910, 977, 1133, 1207, 1312, 1450, and 1598 cm^{-1} (as shown in Figure 8(aii,aiii)). The above-explained Raman spectrum suggests a similar mode of action for PEI-AuNP@Van and voriconazole against conidia. However, detailed molecular mechanisms remain unknown and are currently under investigation.

4.2.2. Raman Spectroscopy Analysis of PEI-AuNP@Van-Treated Conidia of *A. fumigatus*

The Raman spectra of the PEI-AuNP@Van-treated, voriconazole-treated, and untreated conidia of *A. fumigatus* are shown in Figure 8b, and detailed spectrum assignments are shown in Table S1 (Supplementary File). The untreated conidia exhibited several weak intensity peaks between wave numbers 400 and 1200 cm^{-1} ; and a broad and intense peak was observed at 1345 and 1590 cm^{-1} , as shown in Figure 8(bi). The peak assignments can be made based on previously studied biomolecules as follows: 657 cm^{-1} (out-of-plane bending of OH in guanosine/tyrosine), 743 cm^{-1} (CH_2 deformation), 791 cm^{-1} (uracil), 872 cm^{-1} (in-plane bending of CCO in the glucosyl ring), 909 cm^{-1} (stretching in the pyrenoid ring and vibration in CH_2), 1000 cm^{-1} (C–C aromatic ring stretching/breathing

in phenylalanine and galactomannan), 1032–1062 cm^{-1} (C–C stretching in phospholipids and chitin +C–N stretching), 1126 cm^{-1} (C–O–C of unsaturated fatty acids in lipids and galactomannan), and 1152 cm^{-1} (C–O ring, aromatic amino acids in proteins). A broad-spectrum band observed from 1200 to 1650 cm^{-1} was associated with the structural component of a complex polysaccharide and the protein fingerprint of the conidial cell wall in *A. fumigatus*. These features can be assigned to chitin, amide III (random), C–H deformation, galactomannan, CH_2 deformation, C=C stretching, COO symmetrical stretching, amide II, and COO asymmetrical stretching. These spectral bands indicate the intact structure of the conidia.

Similarly, the voriconazole- and PEI-AuNP@Van-treated conidial Raman spectra were recorded, and chemical bonds were assigned to these features. Except for a few peaks, most of the spectral peaks were identical to those of the voriconazole- and PEI-AuNP@Van-treated conidia (Figure 8(bii,biii)). The bands were assigned as follows: 405 cm^{-1} (fructose ring of carbohydrates) and 489 cm^{-1} (C-1-O-C-4 glucoside bond in chitin). Along with overlapping bands, a few shifts were observed in both spectra: 727 to 735 cm^{-1} (cytosine and uracil) and 808 cm^{-1} shifted to 805 cm^{-1} with weakened intensity (antisymmetric stretching in OPO phosphodiester), indicating structural changes in the cell wall component. Furthermore, a band at 1041 cm^{-1} was observed for voriconazole; the spectrum of the PEI-AuNP@Van-treated *A. fumigatus* conidia (Figure 8(aii,aiii)) was similar to that of the *A. flavus* conidia, with a slight shift. However, the spectrum of PEI-AuNP@Van-treated conidia was lower than that of the voriconazole-exposed conidia. The spectra of the PEI-AuNP@Van-treated conidia showed significant differences. For example, extra bands at 1127 and 1199 cm^{-1} (=C–O–C= unsaturated fatty acids within lipids, galactomannan, and chitin) were observed when compared to the spectrum of voriconazole-treated conidia (Figure 8(bii,biii)). This observation indicated a difference in the modes of action of voriconazole and PEI-AuNP@Van at the molecular level. However, the band at 1204 cm^{-1} (in-plane bending in the OH---O +, vibration in C-C, vibration in C-O, and deformation of CH_2) was not observed in the PEI-AuNP@Van-treated conidia, again confirming the differences in the mode of action.

4.3. TEM Analysis

Transmission electron microscopy (TEM) analysis was performed to verify the attachment of the functionalized nanoparticles to the conidial surface and any structural changes associated with PEI-AuNP@Van. The results indicated that the surface interaction dynamics and mechanical impact of PEI-AuNP@Van on the conidia of both *Aspergillus* spp. were distinct (Figure 9). Figure 9a,b illustrates the untreated and PEI-AuNP@Van-treated conidia of *A. fumigatus*, respectively. The conidial architecture was completely disintegrated, and the nanoparticles were attached to fragments of the conidial cell wall (Figure 9b). However, the effect of PEI-AuNP@Van on *A. flavus* conidia differed from that on *A. fumigatus*. Figure 9c,d represent the untreated control and PEI-AuNP@Van-treated conidia of *A. flavus*, respectively. In this case, the functionalized nanoparticles appeared to be attached to the surface but not uniformly, suggesting a sense of binding with specific cell wall domains. Additionally, a brittle crack was observed in the conidial wall, which could be attributed to reactive oxygen species (ROS)-induced cell damage. Moreover, an unusual phenomenon was observed in the PEI-AuNP@Van-treated conidia of *A. flavus*: a thick electron-dense layer was observed on the outer cell wall, and nanoparticles were attached to this layer (Figure S5). This result can be ascribed to the defense mechanism against adverse external conditions.

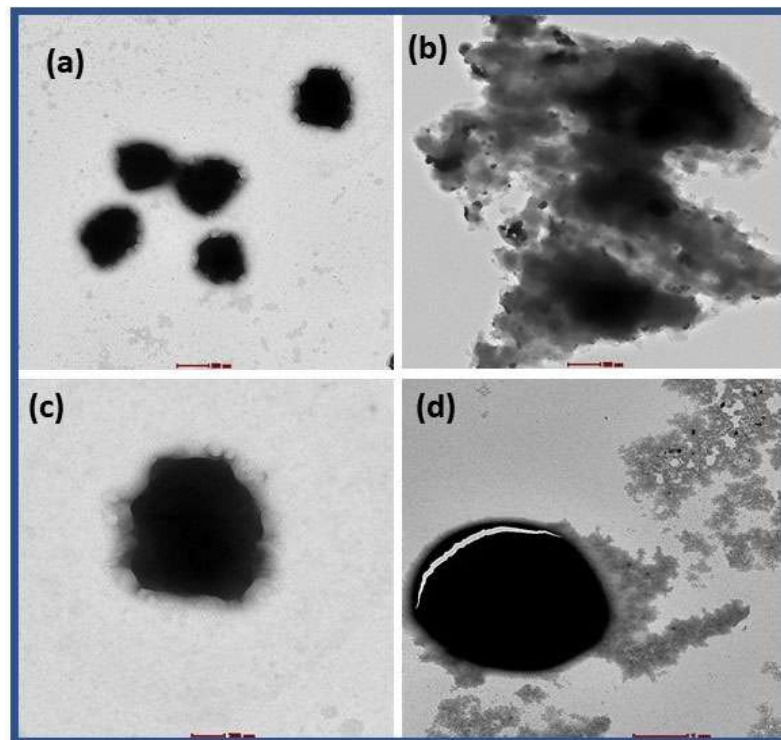


Figure 9. TEM micrograph of PEI-AuNP@Van-treated conidia of *A. fumigatus* and *A. flavus*: (a) represents the untreated conidia of *A. fumigatus*, and (b) treated with PEI-AuNP@Van; (c) represents the untreated conidia of *A. flavus*, and (d) treated with PEI-AuNP@Van.

5. Discussion

Conventionally, Au-NPs are synthesized by reducing HAuCl_4 with citrate and other types of organic reducing agents (e.g., cyclohexanone and 3-glycedoxypropyltrimethoxysilane); their nano geometry can be between 10 and 33 nm [48–50]. Polyethyleneimine (PEI) has been introduced as a stabilizer and reducing agent for metal-nanoparticle synthesis [51,52]. PEI is a cationic polymer used in various industrial applications and drug delivery, especially nucleic acid delivery in mammalian cells [53,54]. However, the previously reported synthetic routes are tedious and time-consuming. We have previously reported a nano-geometry-controlled and rapid synthesis protocol for producing gold and silver nanoparticles using cyclohexanone and formaldehyde as reducing agents, and we evaluated the antimicrobial activity of these materials [55–57]. In this study, we synthesized PEI-stabilized AuNPs and functionalized them with vancomycin. In this procedure, vancomycin interacts with the gold cation in an unusual way that has not been previously reported; however, some previous studies have reported a unique interaction of vancomycin with copper (II) and iridium (III) ions [58,59]. However, the coordination mode associated with the chemical groups interacting with vancomycin and the gold ion remains to be determined without crystals suitable for X-ray structural assignment. The unclear coordination mode may be dependent on the various Lewis bases in vancomycin: the two adjacent, but not consecutive, nitrogen atoms in the amide group and the $-\text{NHCH}_3$ group, the 2, 2'-biphenolic units, the carboxylate on the C-terminus, and the oxygen atom of the asparagine side chain. All of these can potentially serve as coordination sites between vancomycin and the metal center [58,59]. Vancomycin is a glycopeptide with cationic properties and micellar behavior, and it is most likely that PEI participates in the nucleation and stabilization of gold nano geometry. Furthermore, the functionalization of the surface of the gold nanoparticles with vancomycin was confirmed by DLS and fluorescence spectroscopy. An increase in the hydrodynamic radii

compared to bare gold nanoparticles and a shift in the emission maxima (335–418 nm) at the same excitation wavelength (280 nm) confirmed the functionalization (Figures 1 and 2) [33].

Vancomycin exhibits a unique mode of action and is used as an antibacterial agent, mostly against Gram-positive bacteria. It establishes hydrogen bonds with terminal d-alanyl-d-alanine moieties in the NAM/NAG peptides, which prevents the incorporation of the NAM/NAG-peptide subunits within the peptidoglycan matrix [29]. Additionally, there is evidence that vancomycin modifies cell membrane permeability and prevents ribonucleic acid synthesis. Unlike Gram-positive bacteria, the conidial wall of *Aspergillus* has a complex structure composed of unique polysaccharides (chitin, chitosan, galactosaminogalactan, and galactomannan) and glycoproteins (mannoproteins). Galactosaminogalactan comprises α -1-4 linked galactose and α -1-4 linked N-acetyl galactosamine residues [60]. *A. flavus* conidia are heterogeneous in size; they exhibit surface-exposed polysaccharides as well as an amorphous layer that interfaces with the surface rod-let layer. In contrast, *A. fumigatus* conidia exhibited homogeneity in terms of size, with a rod-shaped layer covering their surface. *A. fumigatus* conidia are uniformly covered by the hydrophobic rod-let layer; *A. flavus* conidia exhibit additional amorphous surface patches that are associated with the lowering of hydrophobicity [61]. *A. flavus* conidia contain surface-exposed polysaccharides (e.g., β -1, 3-glucan, α -1, 3-glucan, chitin, and galactomannan) and contain more fibrillary polysaccharides in the cell wall than *A. fumigatus* conidia [61]. The cell walls β -1, 3-glucan content was comparable in the conidia of the two *Aspergillus* species; however, the β -1, 3-glucan of *A. flavus* was more highly branched than that of *A. fumigatus* (as indicated by the higher MIC value). These architectural variations and compositional differences may be associated with the heterogeneity in the killing dynamics of PEI-AuNP@Van against the conidia of *A. fumigatus* and *A. flavus*. Furthermore, *A. flavus* exhibited higher levels of chitin in the cell wall and ergosterol in the cell membrane. It also shows increased peroxidase activity, leading to lower peroxidation of the membrane lipids. Differences in the composition and organization of the conidial cell walls of *A. fumigatus* and *A. flavus* may affect their interactions with PEI-AuNP@Van.

Therefore, studies were undertaken to understand how PEI-AuNP@Van interacts with the conidial surface of *A. fumigatus* and *A. flavus* and the macromolecules responsible for this interaction. Because the conidial cell wall is the first to interact with the PEI-AuNP@Van system, its composition and surface organization may play an important role in the killing kinetics. PEI-functionalized AgNPs have been reported to interact with *C. albicans* surface proteins and sporangiospores on the *R. arrhizus* via electrostatic interactions [36,57]. In this study, the cationic nature of PEI may have enabled binding to the anionic character of the conidia along with vancomycin, leading to vancomycin remaining close to the target macromolecule. As such, the functionalization of vancomycin served as a potent antifungal agent against *A. fumigatus* conidia (free vancomycin did not show any activity per Figure 3a,b). *A. flavus* was less susceptible to PEI-AuNP@Van, as indicated in the MIC study. This result indicates that the structural differences and selective surface binding of PEI-AuNP@Van lead to different results for the two species. Furthermore, PEI-AuNP@Van inhibited the germination of both *Aspergillus* species, and variable dynamics were observed (Figure 4). The conidial susceptibility to PEI-AuNP@Van of *A. fumigatus* (93% germination inhibition) was much higher than that of *A. flavus* (35% inhibition). However, voriconazole only inhibited germination by 56 and 42%, respectively, indicating the germination inhibition potency of PEI-AuNP@Van. Similarly, PI staining revealed the differences in killing dynamics of conidia at 8 h of exposure: 38.4% of *A. fumigatus* conidia were calculated as dead; in contrast, only 28% of conidia of *A. flavus* were calculated as dead (as shown in Figures 5 and 6). These findings support the structural differences between the conidia of the two *Aspergillus* species. To answer this question, we investigated the mechanism underlying

the antifungal activity of PEI-AuNP@Van by using Raman spectroscopy, TEM analysis, and an endogenous ROS generation assay.

ROS are mainly produced in the mitochondria during metabolic redox reactions and are formed as a series of intermediate products during oxygen metabolism. Excessive ROS accumulation degrades intracellular biomolecules (e.g., proteins, lipids, and DNA), leading to irreversible oxidative damage. In this study, we monitored PEI-AuNP@Van-induced ROS production in the conidia of *A. fumigatus* and *A. flavus*. The PEI-AuNP@Van-treated conidia of *A. fumigatus* and *A. flavus* were stained with H₂DCFDA dye, and FACS analysis was performed. We used 2', 7'-dichlorodihydrofluorescein diacetate (H₂DCFDA), a probe that is commonly utilized to measure cellular H₂O₂. Cell-permeable H₂DCFDA diffuses into cells and is deacetylated by cellular esterase to form 2', 7'-dichlorodihydrofluorescein (H₂DCF). In the presence of H₂O₂, H₂DCF is rapidly oxidized to 2', 7'-dichlorofluorescein (DCF), a highly fluorescent molecule, which exhibits an excitation wavelength and emission wavelength of 498 and 522 nm, respectively. The oxidation of H₂DCF to DCF is thought to be specific to H₂O₂, and recent evidence indicates that other ROS (e.g., hydroperoxides, hydroxyl radicals, and peroxyxynitrite) can also oxidize H₂DCF [62]. The PEI-AuNP@Van-treated conidia of *A. flavus* and *A. fumigatus* exhibited variability in ROS generation. Of the conidial population of *A. fumigatus*, 37.4% showed ROS generation after 8 h of exposure to PEI-AuNP@Van; in contrast, the PEI-AuNP@Van-treated conidia of *A. flavus* demonstrated an ROS generation of only 23.1% (as indicated in Figure 7). It is possible that H₂O₂ induces conidial cell death in *A. fumigatus* via a secondary necrosis mechanism [63]. Secondary necrotic cells show a specific morphotype associated with necrotic features (e.g., cytoplasmic membrane rupture) and apoptotic features (e.g., DNA fragmentation). Secondary necrosis is considered to be a form of apoptosis in unicellular eukaryotes. It is associated with cell disintegration and the release of cell components, which takes place when there is no intervention from scavengers, and the entire apoptotic program is completed [63]. However, the conidia of *A. flavus* did not exhibit necrosis-like cell death (Figure 9). This outcome further strengthens previous results regarding the differential modes of action of PEI-AuNP@Van against both *Aspergillus* species.

Raman spectroscopy can be used to analyze biological samples. Raman spectroscopy is a noninvasive, label-free method that is associated with minimal sample preparation and offers information about the structure of complex biological materials. Chemical analysis of the fungal cell wall revealed that proteins and polysaccharides are the main components. Therefore, damage to the cell wall can significantly affect growth and structure, leading to death. Hence, the fungal cell wall is considered an excellent target for the development of antifungal agents [64,65]. Raman spectra of the voriconazole and PEI-AuNP@Van-treated conidia of *A. fumigatus* and *A. flavus*, along with the respective untreated controls, are shown in Figure 8. These results suggest that the modes of action of PEI-AuNP@Van against the conidia of *A. fumigatus* and *A. flavus* are slightly different. In the case of *A. flavus*, most of the peaks are typical of those of voriconazole- and PEI-AuNP@Van-treated conidial spectra (except at 558 and 841 cm⁻¹), as indicated in Figure 8a (ii, iii). These peaks were observed in PEI-AuNP@Van-treated conidia, suggesting the possible binding of vancomycin-functionalized nanoparticles to fructose units and galactomannan components in the cell wall. However, a detailed investigation is required to elucidate the molecular mechanisms of this interaction. The spectral differences among the untreated control, voriconazole-treated, and PEI-AuNP@Van-treated conidia of *A. fumigatus* were similar to those among the conidia of *A. flavus*. The emergence of two new peaks (1127 and 1199 cm⁻¹; =C–O–C= unsaturated fatty acids in lipids, galactomannan, and chitin) in PEI-AuNP@Van-treated conidia again suggests the strong binding of PEI-AuNP@Van with chitin and galactomannan molecules. Hence, it can be concluded that PEI-stabilized Au-NPs act as anchors on the cell walls of conidia and bring vancomycin close to chitin and galactomannan molecules in the PEI-AuNP@Van system. Furthermore, TEM analysis of the PEI-AuNP@Van-treated conidia of *A. flavus* and *A. fumigatus* revealed more severe architectural damage to *A. fumigatus* conidia than to *A. flavus* conidia (Figure

9). This result could be attributed to differences in the cell wall structures of the two species. *A. flavus* conidia have a more branched β -1-3 glucan than *A. fumigatus* conidia, which may inhibit the action of functionalized vancomycin and make it less accessible to target molecules. An unusual phenomenon was observed in the conidial structure of *A. flavus* after exposure to PEI-AuNP@Van. An electron-dense outer layer appeared on the surface of the conidia, which may limit the binding of PEI-AuNP@Van to the cell wall; however, few domains appeared to have access to PEI-AuNP@Van (Figure S5). These results are conclusive and support the structural variation-dependent antifungal activity of PEI-AuNP@Van against the conidia of *A. fumigatus* and *A. flavus*.

6. Conclusions

In summary, the main objective of our study was to understand a novel approach to synthesize vancomycin-functionalized and PEI-stabilized AuNPs for antifungal activity against two filamentous fungi, *A. fumigatus* and *A. flavus*. Our results showed that the synthesized PEI-AuNP@Van exhibited potent antifungal activity against *A. fumigatus*, with a lower MIC value than PEI-AuNPs. However, it demonstrated a high MIC against *A. flavus*. Our findings also indicated that PEI-AuNP@Van attenuated conidial germination by up to 93% and killed up to 38.4% of *A. fumigatus* within 8 h of exposure. In contrast, it only caused a 28% killing of *A. flavus* conidia. The potential mechanism for the differential action of PEI-AuNP@Van against the conidia of *A. fumigatus* and *A. flavus* could be related to the higher amount of fibrillary polysaccharides in *A. flavus*, which may limit the binding of PEI-AuNP@Van. Notably, the molecular differences associated with the cell walls of *A. fumigatus* and *A. flavus* may also play a role in their differential susceptibility. Our study suggests that designing and exploring antifungal drugs against filamentous fungi using efficient delivery systems, such as AuNPs, could be a promising strategy to address emerging antifungal drug resistance.

Supplementary Materials: The following supporting information can be downloaded at: <https://www.mdpi.com/article/10.3390/app14166926/s1>, Figure S1, Optical micrograph of conidial germination inhibition activity of PEI-AuNP@Van and voriconazole along with untreated control against *A. fumigatus*; the data was obtained at several time intervals (i.e., 0, 4, 8, 12, 24, and 48 hours); Figure S2, Optical micrograph of conidial germination inhibition activity of PEI-AuNP@Van and voriconazole along with an untreated control against *A. flavus*; the data was captured at several time intervals (i.e., 0, 4, 8, 12, 24, and 48 hours); Figure S3, Micrographs of live/dead cells. a and b representing the untreated conidia of *A. fumigatus*, (c and d) representing voriconazole-treated conidia, and (e and f) representing PEI-AuNP@Van treated conidia; Figure S4, Live/dead assay by super-resolution confocal microscopy with respective DIC images. a and b representing the untreated control *A. flavus* conidia, (c and d) representing voriconazole-treated conidia, and (e and f) representing PEI-AuNP@Van-treated conidia; Figure S5, TEM micrograph of untreated and PEI-AuNP@Van treated conidia of *A. flavus*, showing an electron-dense outer layer: (a) untreated conidia, and (b) treated with PEI-AuNP@Van; Table S1, Raman spectra of voriconazole and PEI-AuNP@Van treated conidia of *A. flavus* and *A. fumigatus* along with an untreated control and their spectral assignments (+) = Peak Present; (-) = Peak absent.

Author Contributions: A.N. and A.K.T. contributed equally to this work. Conceptualization: A.K.T. and M.K.G.; Data curation: A.K.T. and M.K.G.; Formal analysis: A.K.T.; Funding acquisition: M.K.G.; Investigation: A.N. and A.K.T.; Methodology: A.N., A.K.T., R.T., and M.K.G.; Project administration: M.K.G. and P.C.P.; Resources: M.K.G., P.C.P., S.K., and P.S.B.; Software: A.K.T.; Supervision: M.K.G., P.C.P., and R.J.N.; Validation: A.K.T. and M.K.G.; Visualization: A.N., M.K.G., and P.S.B.; Roles/Writing—original draft: A.K.T.; Writing—review and editing: A.K.T., M.K.G., and R.J.N. All authors have read and agreed to the published version of the manuscript.

Funding: No external funding was received for this work.

Institutional Review Board Statement: Not applicable.

Informed Consent Statement: Not applicable.

Data Availability Statement: The datasets used and/or analyzed in the current study are available in the manuscript and supplementary files.

Acknowledgments: The authors would like to thank the Central Instrument Facility, Indian Institute of Technology (BHU), for the characterization of the nanoparticles, the Central Discovery Centre (CDC), Banaras Hindu University, for providing access to flow cytometry and Raman spectroscopy, and SATHI BHU for Laser scanning super-resolution microscopy. The authors are also thankful to SAIF, AIIMS, New Delhi, India, for TEM imaging of biological samples.

Conflicts of Interest: The authors declare no conflicts of interest.

Abbreviations

PEI-AuNPs	Polyethyleneimine-stabilized gold nanoparticles
PEI-AuNP@Van	Vancomycin-functionalized and polyethyleneimine-stabilized gold nanoparticle
Van	Vancomycin
MIC	Minimum inhibitory concentration
PEI	Polyethyleneimine
µg	Microgram
mL	Microliter
AgNPs	Silver nanoparticles
AuNPs	Gold nanoparticles
TEM	Transmission Electron Microscopy
DLS	Dynamic light scattering
XRD	X-ray diffraction

References

1. Stevens, D.A.; Moss, R.B.; Kurup, V.P.; Knutsen, A.P.; Greenberger, P.; Judson, M.A.; Denning, D.W.; Cramer, R.; Brody, A.S.; Light, M.; et al. Allergic bronchopulmonary aspergillosis in cystic fibrosis—State of the art: Cystic Fibrosis Foundation Consensus Conference. *Clin. Infect. Dis.* **2003**, *37* (Suppl. 3), S225–S264.
2. Denning, D.W.; Pleuvry, A.; Cole, D.C. Global burden of allergic bronchopulmonary aspergillosis with asthma and its complication chronic pulmonary aspergillosis in adults. *Med. Mycol.* **2013**, *51*, 361–370.
3. Denning, D.W.; Pleuvry, A.; Cole, D.C. Global burden of chronic pulmonary aspergillosis as a sequel to pulmonary tuberculosis. *Bull. World Health Organ.* **2011**, *89*, 864–872.
4. Denning, D.W.; Pleuvry, A.; Cole, D.C. Global burden of chronic pulmonary aspergillosis complicating sarcoidosis. *Eur. Respir. J.* **2013**, *41*, 621–626.
5. Rees, J.R.; Pinner, R.W.; Hajjeh, R.A.; Brandt, M.E.; Reingold, A.L. The epidemiological features of invasive mycotic infections in the San Francisco Bay area, 1992–1993: Results of population-based laboratory active surveillance. *Clin. Infect. Dis.* **1998**, *27*, 1138–1147.
6. Vallabhaneni, S.; Benedict, K.; Derado, G.; Mody, R.K. Trends in hospitalizations related to invasive aspergillosis and mucormycosis in the United States, 2000–2013. *Open Forum Infect. Dis.* **2017**, *4*, ofw268.
7. Benedict, K.; Jackson, B.R.; Chiller, T.; Beer, K.D. Estimation of direct healthcare costs of fungal diseases in the United States. *Clin. Infect. Dis.* **2019**, *68*, 1791–1797.
8. Langford, B.J.; So, M.; Raybardhan, S.; Leung, V.; Westwood, D.; MacFadden, D.R.; Soucy, J.P.; Daneman, N. Bacterial coinfection and secondary infection in patients with COVID-19: A living rapid review and meta-analysis. *Clin. Microbiol. Infect.* **2020**, *26*, 1622–1629.
9. Rawson, T.M.; Moore, L.S.; Zhu, N.; Ranganathan, N.; Skolimowska, K.; Gilchrist, M.; Satta, G.; Cooke, G.; Holmes, A. Bacterial and fungal coinfection in individuals with coronavirus: A rapid review to support COVID-19 antimicrobial prescribing. *Clin. Infect. Dis.* **2020**, *71*, 2459–2468.
10. Peng, J.; Wang, Q.; Mei, H.; Zheng, H.; Liang, G.; She, X.; Liu, W. Fungal coinfection in COVID-19 patients: Evidence from a systematic review and meta-analysis. *Aging* **2021**, *13*, 7745.
11. Falcone, M.; Tiseo, G.; Giordano, C.; Leonildi, A.; Menichini, M.; Vecchione, A.; Pistello, M.; Guarracino, F.; Ghiadoni, L.; Forfori, F.; et al. Predictors of hospital-acquired bacterial and fungal superinfections in COVID-19: A prospective observational study. *J. Antimicrob. Chemother.* **2021**, *76*, 1078–1084.
12. Lai, C.C.; Yu, W.L. COVID-19 associated with pulmonary aspergillosis: A literature review. *J. Microbiol. Immunol. Infect.* **2021**, *54*, 46–53.
13. Villanueva-Lozano, H.; Treviño-Rangel, R.D.; González, G.M.; Ramírez-Elizondo, M.T.; Lara-Medrano, R.; Aleman-Bocanegra, M.C.; Guajardo-Lara, C.E.; Gaona-Chávez, N.; Castilleja-Leal, F.; Torre-Amione, G.; et al. Outbreak of *Candida auris* infection in a COVID-19 hospital in Mexico. *Clin. Microbiol. Infect.* **2021**, *27*, 813–816.

14. Centre for Disease Control and Prevention. Antimicrobial Resistant—Aspergillus. Available online: <https://www.cdc.gov/fungal/diseases/aspergillosis/antifungal-resistant.html> (accessed on 1 July 2024).
15. Gupta, M.K.; Chandra, A.; Prakash, P.; Tilak, R. Necessity to identify the causative agent for appropriate treatment in fungal corneal ulcer: An in vitro study. *J. De Mycol. Médicale* **2018**, *28*, 201–205.
16. Lestrade, P.P.; Bentvelsen, R.G.; Schauwvlieghe, A.F.; Schalekamp, S.; van der Velden, W.J.; Kuiper, E.J.; van Paassen, J.; van der Hoven, B.; van der Lee, H.A.; Melchers, W.J.; et al. Voriconazole resistance and mortality in invasive aspergillosis: A multicenter retrospective cohort study. *Clin. Infect. Dis.* **2019**, *68*, 1463–1471.
17. Wang, L.; Hu, C.; Shao, L. The antimicrobial activity of nanoparticles: Present situation and prospects for the future. *Int. J. Nanomed.* **2017**, *12*, 1227–1249.
18. Gao, W.; Thamphiwatana, S.; Angsantikul, P.; Zhang, L. Nanoparticle approaches against bacterial infections. *Wiley Interdiscip. Rev. Nanomed. Nanobiotechnol.* **2014**, *6*, 532–547.
19. Lee, N.Y.; Ko, W.C.; Hsueh, P.R. Nanoparticles in the treatment of infections caused by multidrug-resistant organisms. *Front. Pharmacol.* **2019**, *10*, 1153.
20. Vassallo, A.; Silletti, M.F.; Faraone, I.; Milella, L. Nanoparticulate antibiotic systems as antibacterial agents and antibiotic delivery platforms to fight infections. *J. Nanomater.* **2020**, *2020*, 6905631.
21. Sánchez-López, E.; Gomes, D.; Esteruelas, G.; Bonilla, L.; Lopez-Machado, A.L.; Galindo, R.; Cano, A.; Espina, M.; Ettcheto, M.; Camins, A.; et al. Metal-based nanoparticles as antimicrobial agents: An overview. *Nanomaterials* **2020**, *10*, 292.
22. Bankier, C.; Matharu, R.K.; Cheong, Y.K.; Ren, G.G.; Cloutman-Green, E.; Ciric, L. Synergistic antibacterial effects of metallic nanoparticle combinations. *Sci. Rep.* **2019**, *9*, 16074.
23. Li, W.; Cao, Z.; Liu, R.; Liu, L.; Li, H.; Li, X.; Chen, Y.; Lu, C.; Liu, Y. AuNPs as an important inorganic nanoparticle applied in drug carrier systems. *Artif. Cells Nanomed. Biotechnol.* **2019**, *47*, 4222–4233.
24. Okkeh, M.; Bloise, N.; Restivo, E.; De Vita, L.; Pallavicini, P.; Visai, L. Gold nanoparticles: Can they be the next magic bullet for multidrug-resistant bacteria? *Nanomaterials* **2021**, *11*, 312.
25. Al Saqr, A.; Khafagy, E.S.; Alalaiwe, A.; Aldawsari, M.F.; Alshahrani, S.M.; Anwer, M.K.; Khan, S.; Lila, A.S.; Arab, H.H.; Hegazy, W.A. Synthesis of gold nanoparticles by using green machinery: Characterization and in vitro toxicity. *Nanomaterials* **2021**, *11*, 808.
26. Lee, B.; Lee, D.G. Synergistic antibacterial activity of gold nanoparticles caused by apoptosis-like death. *J. Appl. Microbiol.* **2019**, *127*, 701–712.
27. Fuller, M.; Whiley, H.; Köper, I. Antibiotic delivery using gold nanoparticles. *SN Appl. Sci.* **2020**, *2*, 1022.
28. Rahimi, H.; Roudbarmohammadi, S.; Delavari, H.H.; Roudbary, M. Antifungal effects of indolicidin-conjugated gold nanoparticles against fluconazole-resistant strains of *Candida albicans* isolated from patients with burn infection. *Int. J. Nanomed.* **2019**, *14*, 5323–5338.
29. Watanakunakorn, C. Mode of action and in-vitro activity of vancomycin. *J. Antimicrob. Chemother.* **1984**, *14* (Suppl. D), 7–18.
30. Ku, T.S.; Palanisamy, S.K.; Lee, S.A. Susceptibility of *Candida albicans* biofilms to azithromycin, tigecycline and vancomycin and the interaction between tigecycline and antifungals. *Int. J. Antimicrob. Agents* **2010**, *36*, 441–446.
31. Singh, R.; Shivaprakash, M.R.; Chakrabarti, A. Biofilm formation by zygomycetes: Quantification, structure and matrix composition. *Microbiology* **2011**, *157*, 2611–2618.
32. Pandey, P.C.; Pandey, G.; Narayan, R.J. Controlled synthesis of Polyethyleneimine coated gold nanoparticles: Application in glutathione sensing and nucleotide delivery. *J. Biomed. Mater. Res. Part B Appl. Biomater.* **2017**, *105*, 1191–1199.
33. Tiwari, A.K.; Yadav, H.P.; Gupta, M.K.; Narayan, R.J.; Pandey, P.C. Synthesis of vancomycin functionalized fluorescent gold nanoparticles and selective sensing of mercury (II). *Front. Chem.* **2023**, *11*, 1238631.
34. CLSI. Method for Antifungal Disk Diffusion Susceptibility Testing of Non dermatophyte Filamentous Fungi. In *Approved Guideline, CLSI Document M51-A*; Clinical and Laboratory Standards Institute: Wayne, PA, USA, 2010.
35. Chen, J.; Peng, H.; Wang, X.; Shao, F.; Yuan, Z.; Han, H. Graphene oxide exhibits broad-spectrum antimicrobial activity against bacterial phytopathogens and fungal conidia by intertwining and membrane perturbation. *Nanoscale* **2014**, *6*, 1879–1889.
36. Tiwari, A.K.; Gupta, M.K.; Pandey, G.; Tilak, R.; Narayan, R.J.; Pandey, P.C. Size and zeta potential clicked germination attenuation and anti-sporangiospores activity of PEI-functionalized silver nanoparticles against COVID-19 associated Mucorales (*Rhizopus arrhizus*). *Nanomaterials* **2022**, *12*, 2235.
37. Singh, A.K.; Yadav, S.; Sharma, K.; Firdaus, Z.; Aditi, P.; Neogi, K.; Bansal, M.; Gupta, M.K.; Shanker, A.; Singh, R.K.; et al. Quantum curcumin mediated inhibition of gingipains and mixed-biofilm of *Porphyromonas gingivalis* causing chronic periodontitis. *RSC Adv.* **2018**, *8*, 40426–40445.
38. Zając, A.; Hanuza, J.; Wandas, M.; Dymińska, L. Determination of N-acetylation degree in chitosan using Raman spectroscopy. *Spectrochim. Acta Part A Mol. Biomol. Spectrosc.* **2015**, *134*, 114–120.
39. De Gelder, J.; De Gussem, K.; Vandenabeele, P.; Moens, L. Reference database of Raman spectra of biological molecules. *J. Raman Spectrosc. Int. J. Orig. Work All Asp. Raman Spectrosc. Incl. High. Order Process. Also Brillouin Rayleigh Scatt.* **2007**, *38*, 1133–1147.
40. Freire, P.T.; Barboza, F.M.; Lima, J.A.; Melo, F.E.; Mendes Filho, J. Raman spectroscopy of amino acid crystals. *Raman Spectrosc. Appl.* **2017**, *201*, 171.
41. Xia, J.; Li, W.; Sun, M.; Wang, H. Application of SERS in the Detection of Fungi, Bacteria and Viruses. *Nanomaterials* **2022**, *12*, 3572.

42. Raza, A.; Parveen, S.; Majeed, M.I.; Nawaz, H.; Javed, M.R.; Iqbal, M.A.; Rashid, N.; Haider, M.Z.; Ali, M.Z.; Sabir, A.; et al. Surface-enhanced Raman spectral characterization of antifungal activity of selenium and zinc based organometallic compounds. *Spectrochim. Acta Part A Mol. Biomol. Spectrosc.* **2023**, *285*, 121903.
43. Witkowska, E.; Jagielski, T.; Kamińska, A.; Kowalska, A.; Hrynciewicz-Gwóźdź, A.; Waluk, J. Detection and identification of human fungal pathogens using surface-enhanced Raman spectroscopy and principal component analysis. *Anal. Methods* **2016**, *8*, 8427–8434.
44. Hu, H.; Wang, J.; Yi, X.; Lin, K.; Meng, S.; Zhang, X.; Jiang, C.; Tang, Y.; Wang, M.; He, J.; et al. Stain-free Gram staining classification of pathogens via single-cell Raman spectroscopy combined with machine learning. *Anal. Methods* **2022**, *14*, 4014–4020.
45. Sujith, A.; Itoh, T.; Abe, H.; Yoshida, K.I.; Kiran, M.S.; Biju, V.; Ishikawa, M. Imaging the cell wall of living single yeast cells using surface-enhanced Raman spectroscopy. *Anal. Bioanal. Chem.* **2009**, *394*, 1803–1809.
46. Assmann, C.; Kirchoff, J.; Beleites, C.; Hey, J.; Kostudis, S.; Pfister, W.; Schlattmann, P.; Popp, J.; Neugebauer, U. Identification of vancomycin interaction with *Enterococcus faecalis* within 30 min of interaction time using Raman spectroscopy. *Anal. Bioanal. Chem.* **2015**, *407*, 8343–8352.
47. Neugebauer, U.; Rösch, P.; Schmitt, M.; Popp, J.; Julien, C.; Rasmussen, A.; Budich, C.; Deckert, V. On the way to nanometer-sized information of the bacterial surface by tip-enhanced Raman spectroscopy. *Chemphyschem Eur. J. Chem. Phys. Phys. Chem.* **2006**, *7*, 1428–1430.
48. Rak, M.J.; Saadé, N.K.; Friščić, T.; Moores, A. Mechanosynthesis of ultra-small monodisperse amine-stabilized gold nanoparticles with controllable size. *Green Chem.* **2014**, *16*, 86–89.
49. Mitra, M.D.; Pandey, P.C. Functional trialkoxysilane mediated controlled synthesis of fluorescent gold nanoparticles and fluorometric sensing of dopamine. *Opt. Mater.* **2022**, *132*, 112810.
50. Pandey, P.C.; Tiwari, A.K.; Gupta, M.K.; Pandey, G.; Narayan, R.J. Effect of the organic functionality on the synthesis and antimicrobial activity of silver nanoparticles. *Nano Life* **2020**, *10*, 2050002.
51. Kim, E.J.; Yeum, J.H.; Choi, J.H. Effects of polymeric stabilizers on the synthesis of gold nanoparticles. *J. Mater. Sci. Technol.* **2014**, *30*, 107–111.
52. Cho, T.J.; Gorham, J.M.; Pettibone, J.M.; Liu, J.; Tan, J.; Hackley, V.A. Parallel multi-parameter study of PEI-functionalized gold nanoparticle synthesis for bio-medical applications: Part 1—A critical assessment of methodology, properties, and stability. *J. Nanopart. Res.* **2019**, *21*, 188.
53. Li, A.; Qiu, J.; Zhou, B.; Xu, B.; Xiong, Z.; Hao, X.; Shi, X.; Cao, X. The gene transfection and endocytic uptake pathways mediated by PEGylated PEI-entrapped gold nanoparticles. *Arab. J. Chem.* **2020**, *13*, 2558–2567.
54. Jin, Y.; Adams, F.; Möller, J.; Isert, L.; Zimmermann, C.M.; Keul, D.; Merkel, O.M. Synthesis and Application of Low Molecular Weight PEI-Based Copolymers for siRNA Delivery with Smart Polymer Blends. *Macromol. Biosci.* **2023**, *23*, 2200409.
55. Pandey, P.C.; Pandey, G.; Narayan, R.J. Polyethylenimine-mediated synthetic insertion of gold nanoparticles into mesoporous silica nanoparticles for drug loading and biocatalysis. *Biointerphases* **2017**, *12*, 011005.
56. Pandey, P.C.; Pandey, G. Synthesis of gold nanoparticles resistant to pH and salt for biomedical applications; functional activity of organic amine. *J. Mater. Res.* **2016**, *31*, 3313–3323.
57. Tiwari, A.K.; Gupta, M.K.; Narayan, R.J.; Pandey, P.C. A whole cell fluorescence quenching-based approach for the investigation of polyethylenimine functionalized silver nanoparticles interaction with *Candida albicans*. *Front. Microbiol.* **2023**, *14*, 1131122.
58. Facchetti, G.; Pellegrino, S.; Bucci, R.; Nava, D.; Gandolfi, R.; Christodoulou, M.S.; Rimoldi, I. Vancomycin-Iridium (III) Interaction: An Unexplored Route for Enantioselective Imine Reduction. *Molecules* **2019**, *24*, 2771.
59. Świątek, M.; Valensin, D.; Migliorini, C.; Gaggelli, E.; Valensin, G.; Jeżowska-Bojczuk, M. Unusual binding ability of vancomycin towards Cu²⁺ ions. *Dalton Trans.* **2005**, *23*, 3808–3813.
60. Fontaine, T.; Delangle, A.; Simenel, C.; Coddeville, B.; van Vliet, S.J.; Van Kooyk, Y.; Bozza, S.; Moretti, S.; Schwarz, F.; Trichot, C.; et al. Galactosaminogalactan, a new immunosuppressive polysaccharide of *Aspergillus fumigatus*. *PLoS Pathog.* **2011**, *7*, e1002372.
61. Wong, S.S.; Venugopalan, L.P.; Beaussart, A.; Karnam, A.; Mohammed, M.R.; Jayapal, J.M.; Bretagne, S.; Bayry, J.; Prajna, L.; Kuppamuthu, D.; et al. Species-specific immunological reactivities depend on the cell-wall organization of the two *Aspergillus*, *Aspergillus fumigatus* and *A. flavus*. *Front. Cell. Infect. Microbiol.* **2021**, *11*, 643312.
62. Eruslanov, E.; Kusmartsev, S. Identification of ROS using oxidized DCFDA and flow-cytometry. *Adv. Protoc. Oxidative Stress II* **2010**, *594*, 57–72.
63. Oliveira, M.; Pereira, C.; Bessa, C.; Araujo, R.; Saraiva, L. Hydrogen peroxide-induced secondary necrosis in conidia of *Aspergillus fumigatus*. *Can. J. Microbiol.* **2016**, *62*, 95–101.
64. Ruiz-Herrera, J. *Fungal Cell Wall: Structure, Synthesis, and Assembly*; CRC: Boca Raton, FL, USA, 1991.
65. Bowman, S.M.; Free, S.J. The structure and synthesis of the fungal cell wall. *Bioassays* **2006**, *28*, 799–808.

Disclaimer/Publisher's Note: The statements, opinions and data contained in all publications are solely those of the individual author(s) and contributor(s) and not of MDPI and/or the editor(s). MDPI and/or the editor(s) disclaim responsibility for any injury to people or property resulting from any ideas, methods, instructions or products referred to in the content.